

Statistical properties of global significant wave heights and their use for validation

Eva Bauer

Potsdam Institute for Climate Impact Research, Potsdam, Germany

Christoph Staabs

Institut für Meereskunde, Universität Hamburg, Hamburg, Germany

Abstract. Global data sets of significant wave height (H_s) from altimeter measurements and from the wave model WAM are analyzed statistically to assess the quality of the data. H_s derived from the altimeters aboard Seasat (1978), Geosat (1988), ERS-1 (1993, 1994), and TOPEX (1993, 1994) and from WAM (1988, 1993) and, in addition, from in situ data of Ocean Weather Station M in the North Atlantic are used. First, collocated data sets are compared through linear regression and principal component analysis. From this, a good agreement between H_s of the ERS-1 altimeter (1993) and the WAM model is inferred. Second, the H_s frequency distributions are described by the first four moments. Using the first four moments of linear order statistics, the lognormal and the general extreme value distribution function are found to approximate distributions of H_s best. H_s from Seasat and ERS-1 (1993) deviate from these empirical distribution functions, manifesting weaknesses in the data. Although H_s from ERS-1 have weaknesses, their assimilation into WAM has a positive impact. The assessment of the quality of this existing H_s data provides a prerequisite for the coming assimilation schemes using wave data from synthetic aperture radars and also for climate research studies.

1. Introduction

The prediction of the global sea state with large accuracy is presently gaining importance. One aspect is to provide reliable forecasts some days in advance to plan ship routes and offshore activities optimally. Another aspect is to determine the wave climate on decadal timescales to investigate possible changes.

The energy of ocean waves is conventionally represented by the significant wave height (H_s). H_s is either defined as the mean over the upper third of sorted wave heights (from trough to crest) or as $H_s = 4\sqrt{E}$, where E represents the integral over the wave variance spectrum. In the past, point measurements of H_s were inferred from time series of sea surface elevations obtained by gauges and buoys. Since the advent of spaceborne radar altimeters, H_s is measured globally. Radar altimeters are active microwave sensors which operate during all weather conditions. H_s is inferred directly from the shape of the radar pulse returning to the nadir looking altimeter assuming Gaussian surface elevations [Barrick, 1968]. The accuracy of H_s from altimeters was repeatedly confirmed to fall below the specified er-

ror bounds of 0.5 m or 10%, whichever is larger in the range 1 to 20 m [e.g., Callahan *et al.*, 1994].

In parallel to the measurement approach, dynamic models predicting ocean wave fields have been developed progressively [Komen *et al.*, 1994]. Nowadays, the spectral third-generation Wave Model (WAM) [WAMDI Group, 1988] is running routinely at the European Centre for Medium-Range Weather Forecasts (ECMWF) and also in many other operational weather centers. In the following we will assess the quality of global H_s data sets obtained from the altimeters of the satellites Seasat, Geosat, ERS-1, and TOPEX, and from the WAM model through a combined statistical analysis. Hereafter, these global data sets are abbreviated H_s^S , H_s^G , H_s^E , H_s^T , and H_s^W , respectively.

A recent comparison of global H_s for 1993 showed that the means of H_s^T and H_s^E from the range of 0.5 to 13 m agreed reasonably with H_s^W [Staabs, 1994]. A regression analysis of the global H_s data sets suggested that H_s^W underestimates (overestimates) high (low) sea states compared with H_s^T . The comparison of H_s^W with H_s^E showed the reverse. The global monthly means of H_s^W differed by less than 0.15 m against H_s^E and H_s^T , but regional differences ranged from -0.5 to 1 m. In the tropical Pacific, means of H_s^T and H_s^E were generally slightly smaller than those of H_s^W , but this is different in the tropical Atlantic. In the central North

Copyright 1998 by the American Geophysical Union.

Paper number 97JC02568.
0148-0227/97/98JC-02568\$09.00

Atlantic, in January 1993, the mean H_s^W was 0.5 m higher than the mean H_s^E , but H_s^W was 0.5 m smaller than H_s^T . Remarkable differences were also observed in the southern Indian Ocean in July 1993, giving an inhomogeneous picture of the differences in space and time. The question arises which of the H_s data sets represent the true sea state more closely? Do we have to seek for shortcomings in the measurement, or in the modeling approach, or in both?

A previous comparison of H_s^W with H_s^S from August 1978 indicated that most of the deviations, in particular, in the strong wind regions, could be ascribed to shortcomings in the modeling [Bauer et al., 1992]. WAM underestimated H_s in the southern regions because the wind stresses driving the wave model were too low.

Romeiser [1993] analyzed H_s^W collocated to H_s^G for 1988. The overall agreement between the monthly means of H_s^W and H_s^G was rather good. Large deviations were seen only in the Indian monsoon region and in the area around the Indonesian archipelago.

Hansen and Günther [1992] validated the ERS-1 fast delivery product (FDP) H_s against H_s^W . The globally collocated data from November 30 to December 28, 1991, shared a correlation coefficient of 0.89. They concluded from the regression analysis that the FDP from H_s^E underestimated high sea states.

Many studies are concerned with validating H_s from altimeters against ground truth observations from buoys and ships. Fedor and Brown [1982] found a small mean difference of 0.07 m between H_s^S and buoy data with rms error of 0.29 m for H_s ranging from 0.5 to 5.0 m. H_s from ship reports in the North Atlantic as large as 8 m were about 0.2 m smaller than H_s^S with a rms error of 0.8 m [Queffelec, 1983]. H_s^G was biased low by 0.36 m with a rms error of 0.49 m compared to H_s from 43 buoys of the U.S. National Data Buoy Center (NDBC) Network based on 116 data points having H_s up to 6 m [Dobson et al., 1987]. Also, Tournadre and Ezraty [1990] inferred an underestimation of H_s^G from a 2-year time series of in situ measurements at an oil platform in the North Sea. The mean difference was 0.23 m, and the rms error 0.47 m, taking H_s^G within a radius of 100 km from the oil platform. Carter et al. [1992] inferred from 164 closely collocated data points that H_s^G was 13% smaller than H_s from NDBC buoys. This study included only four entries with H_s larger than 6 m.

During the ERS-1 Calibration/Validation Campaign the FDP from H_s^E and H_s from TOBIS buoys showed a high correlation coefficient of 0.98 [Queffelec and Lefevre, 1992]. The linear regression line having slope 0.84 and intercept 0.37 m was based on only 13 data points. The TOBIS buoys were cross validated two by two showing maximum differences in long-term averages of 0.22 m and standard deviations of less than 0.1 m [Queffelec and Bentamy, 1992].

Cotton and Carter [1994] calculated monthly means for latitude-longitude boxes of $2^\circ \times 2^\circ$ from H_s^G , H_s^E ,

and H_s^T , and from H_s of NDBC buoys. The means of H_s^G were from October 1985 to December 1988, while the means of H_s^E and H_s^T , and of the buoys were from October 1992 to September 1993. H_s^G was increased by 13% following Carter et al. [1992]. Both the FDP and the off-line (OPR) data of ERS-1 altimeter were smaller than H_s^T . The scattering between H_s^E and H_s^T with respect to H_s^G from the same month but five years apart was attributed to interannual variability. Cotton and Carter [1994] adjusted FDP of H_s^E , OPR of H_s^E , and H_s^T with linear correction functions inferred from buoy data. The correction functions were based on 24 buoys with means smaller than 5 m. This adjustment was found to lead to a better agreement between the shapes of the histograms.

Callahan et al. [1994] compared H_s histograms from six months (January to June). The histogram of H_s^T from 1993 was shifted by as much as 0.3 m to larger values with respect to the histogram of H_s^G averaged over 1987 to 1989. The recent work of Gower [1996] shows that H_s of TOPEX and of buoys in the NE Pacific from September 1992 to December 1993 agree well in the range 0.1 to 8 m. On average H_s^T is low by 5%.

No definite conclusion can be drawn yet which of the global H_s data sets is closest to the true sea state. In part, this is due to the relatively small number of collocations of satellite and ground truth data through which the natural range of H_s is covered only incompletely. Furthermore, the validation of H_s from altimeters with buoy measurements can be affected by errors from the instruments, the temporal and spatial proximity, and approximations in the geophysical model function [Monaldo, 1988]. The wave model WAM is a useful tool for the validation of H_s data. However, model calculations are also limited in reproducing the observations perfectly which is largely caused by insufficient computer resources. Wave and atmosphere models use relative coarse spatial grids and rely on parameterizations. Errors in wave modeling are mainly caused by errors in wind forcing [Zambresky, 1991; Cardone et al., 1995] which can be corrected by data assimilation techniques [e.g., Lionello et al., 1995; Bauer et al., 1996]. To assess the quality of H_s data, some general quality criteria are needed which we will pursue here.

In section 2 we describe the data sets used. The bivariate distributions of H_s from collocating altimeter and model data are characterized by linear regression and principal component analysis in section 3. Section 4 deals with the properties of the frequency distribution of H_s . Using monthly moments of linear order statistics, appropriate theoretical distribution functions are determined. Section 5 draws conclusions on the assessment of the quality of the various data sets.

2. Data Sets of H_s

Modeled H_s are obtained from the wave model WAM running on a global $3^\circ \times 3^\circ$ grid. The WAM model is driven by 6-hourly wind fields from the ECMWF

model. Fields of H_s are stored every 6 hours. As the WAM model has been changed progressively in the past years, this study involves data from WAM cycle 3 and cycle 4. Cycle 4 now includes the dynamic coupling between the wave-induced stress and the atmospheric stress [Janssen, 1991].

Observed H_s from altimeters aboard the satellites Seasat (July 1978 to September 1978), Geosat (1988), ERS-1 (1993 - 1994), and TOPEX (1993 - 1994) are prepared by the same quality analysis and averaging procedure [see Bauer *et al.*, 1992; Romeiser, 1993; Staabs, 1994]. We analyze the FDP of H_s^E instead of the OPR data because we are interested particularly in the quality of the FDP data as they are used in the operational wave data assimilation scheme. From the altimeter measurements along-track means over 30 s are calculated. This corresponds to a spatial resolution of about 200 km in accordance with the spatial model resolution but is still finer in time. Collocated sets of H_s are determined by trilinear interpolation (two in space and one in time) of the WAM data to the Geosat, the ERS-1, and the TOPEX altimeter data. H_s^G is collocated to H_s^W of cycle 3, and H_s^E and H_s^T to H_s^W of cycle 4. Since August 16, 1993, H_s^W is updated by the ECMWF assimilation scheme using H_s^E .

In addition, we use in situ measured H_s from Ocean Weather Station (OWS) M in the North Atlantic (66°N, 2°E). The time series from 1949 to 1993 consists of 15,000 samples of daily mean values. These data can be regarded homogeneous for the purpose of this study.

Table 1 summarizes the time periods covered by the different data sets. The outer latitudinal boundaries depend on the different satellite orbits and on the model grid. Data from areas with sea-ice were excluded. Since August 1993, the WAM model uses actual ice boundaries inferred from sea surface temperature analyses provided by the National Center for Environmental Prediction (NCEP).

3. Statistics of Bivariate Distributions of H_s

3.1. General Considerations

Collocated data sets of H_s are commonly displayed in a scatter diagram. The abscissa is assigned to the independent variable x which is supposed to be known exactly. The ordinate represents the dependent variable y accompanied by random uncertainty. The linear dependence between the data sets is described by the regression line

$$\hat{y} = b_{yx}x + a_{yx} \quad (1)$$

where b_{yx} is the slope, a_{yx} is the intercept on the y axis, and \hat{y} arises from the straight line fit. The slope

$$b_{yx} = \frac{s_{yx}}{s_{xx}} \quad (2)$$

and the intercept

$$a_{yx} = \langle y \rangle - b_{yx} \langle x \rangle \quad (3)$$

depend on the covariance $s_{yx} = s_{xy} = \langle (y - \langle y \rangle)(x - \langle x \rangle) \rangle$ and the variance $s_{xx} = \langle (x - \langle x \rangle)^2 \rangle$ where angle brackets denote the ensemble mean.

If y and x are both variables with random noise, then the second regression line from interchanging x and y is useful for comparison. The second line defined in the above coordinate system is

$$y = b_{xy}\hat{x} + a_{xy} \quad (4)$$

The slope b_{xy} is given by

$$b_{xy} = \frac{s_{yy}}{s_{yx}} \quad (5)$$

where s_{yy} is the variance of y and the intercept on the y axis is derived analogously to (3). The regression lines cross in the center point of the data defined by $\langle x \rangle$ and $\langle y \rangle$.

If x and y lie exactly on a straight line, then the correlation coefficient r

$$r = \frac{s_{yx}}{\sqrt{s_{xx}s_{yy}}} \quad (6)$$

is either $r = 1$ or $r = -1$ and both regression lines are identical. The regression lines deviate with increasing noise while the magnitude of r decreases.

Linear transformations applied to x , as $x^* = c_1x + c_0$, or/and to y , as $y^* = d_1y + d_0$ leave r unchanged (provided the scale factors c_1 and d_1 have equal signs). But r depends on the signal-to-noise ratio and slightly on the slope of the regression line. The functional dependencies of r become evident from substituting $y = bx + a + \varepsilon$ into (6). The noise is denoted by ε . Then r reads as a function of b

$$r(b) = \frac{bs_{xx} + \langle x\varepsilon \rangle}{[b^2s_{xx}^2 + 2bs_{xx}\langle x\varepsilon \rangle + s_{xx}\langle \varepsilon^2 \rangle]^{1/2}} \quad (7)$$

If ε may be regarded as uncorrelated with x , then $\langle x\varepsilon \rangle \approx 0$. Thus (7) reduces to

$$r(b) \approx \frac{b}{[b^2 + \langle \varepsilon^2 \rangle / s_{xx}]^{1/2}} \quad (8)$$

Table 1. Area and Period of used H_s Data Sets with WAM collocated to corresponding altimeter data

Data Set	Area	Period
Seasat	78°N - 60°S	July 7 to Oct. 10, 1978
WAM - Geosat	69°N - 60°S	Jan. 1 to Dec. 31, 1988
WAM - ERS-1	69°N - 60°S	Jan. 1 to July 31, 1993
WAM - ERS-1	78°N - 78°S*	Aug. 1 to Dec. 31, 1993
ERS-1	78°N - 78°S*	Jan. 1 to Dec. 31, 1994
WAM - TOPEX	66°N - 60°S	Jan. 1 to July 31, 1993
WAM - TOPEX	66°N - 66°S*	Aug. 1 to Dec. 31, 1993
TOPEX	66°N - 66°S*	Jan. 1 to Dec. 31, 1994
OWS M	2°E, 66°N	1949 to 1993

* Latitudinal range is adapted to actual ice boundary.

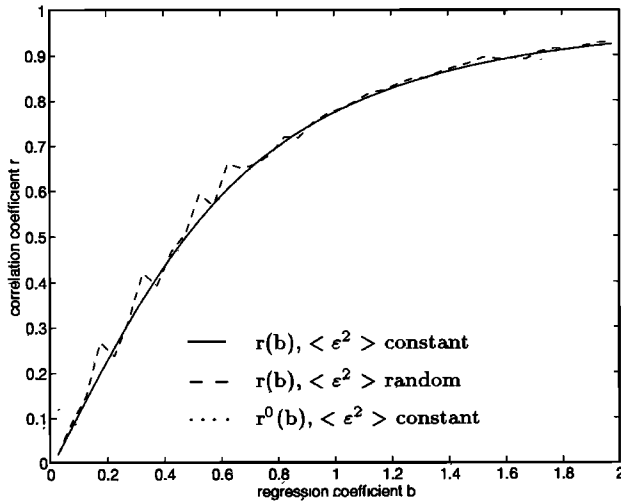


Figure 1. Correlation coefficient r as function of slope b with $\langle \varepsilon^2 \rangle = 1 \text{ m}^2$. Solid line represents $\langle \varepsilon^2 \rangle$ chosen once; dashed line is $\langle \varepsilon^2 \rangle$ chosen randomly and independently for each evaluation of r , and dotted line is r^0 (13) as function of slope b .

The correlation coefficient increases as $\langle \varepsilon^2 \rangle / s_{xx}$ decreases. When the signal-to-noise ratio is kept constant, then r grows from -1 to $+1$, with b growing from $-\infty$ to $+\infty$. For example, the correlation coefficient r (8) grows from 0 to 0.93, with b growing from 0 to 2 when x has distribution properties typical for H_s , and when the noise is normally distributed with $\langle \varepsilon^2 \rangle = 1 \text{ m}^2$ and $\langle \varepsilon \rangle = 0 \text{ m}$ (Figure 1). Qualitatively, this result is independent of the underlying population distribution. The same, but nonmonotonic curve is obtained when ε is chosen randomly for each evaluation of r . The growth of r with b also implies that r grows with bias $d = \langle y \rangle - \langle x \rangle$.

The combination of the regression lines (1) and (4) yields the so-called symmetric regression line

$$\hat{y}_s = b_s x + a_s \quad (9)$$

where the slope

$$b_s = \sqrt{b_{yx} b_{xy}} = \sqrt{\frac{s_{yy}}{s_{xx}}} \quad (10)$$

represents the geometric mean of (2) and (5), and a_s denotes the intercept with the y axis [see Cotton and Carter, 1994]. The symmetric regression line passes also through the center point and bisects the angle between the above regression lines.

For some applications the regression line passing through the origin of the coordinate system might be appropriate. The regression line is given by

$$\hat{y}^0 = b_{yx}^0 x \quad (11)$$

with slope

$$b_{yx}^0 = \frac{\langle xy \rangle}{\langle x^2 \rangle} \quad (12)$$

The linear regression analysis between H_s^G and H_s of the NDBC buoys performed by Carter *et al.* [1992] was based on (11). The slope was estimated as $b_{yx}^0 = 1.13$, leading to the conclusion that H_s^G was low by 13%. The corresponding correlation coefficient r^0 [Bauer *et al.*, 1992] is given by

$$r^0 = \frac{\langle xy \rangle}{\sqrt{\langle x^2 \rangle \langle y^2 \rangle}} \quad (13)$$

Its slope dependence is shown for comparison in Figure 1.

A superior method to characterize a bivariate data distribution is the principal component analysis. The principal component analysis yields the major and minor axis of the elliptical distribution. These axes also cross in the center point. The first and the second eigenvalue of the data covariance matrix represent the maximum and minimum variance along the axes. The major axis $\hat{y}_p = b_p x + a_p$ has the slope

$$b_p = \tan \Theta \quad (14)$$

where Θ is the first principal angle

$$\Theta = \frac{1}{2} \arctan \frac{2s_{xy}}{s_{xx} - s_{yy}} \quad (15)$$

and a_p is the intercept on the y axis. The principal rms deviations σ_{p1} and σ_{p2} , i.e., the square roots of the eigenvalues, are

$$\left. \begin{array}{l} \sigma_{p1} \\ \sigma_{p2} \end{array} \right\} = \left(\frac{1}{2} \left\{ (s_{xx} + s_{yy}) \pm [(s_{xx} - s_{yy})^2 + 4s_{xy}^2]^{\frac{1}{2}} \right\} \right)^{\frac{1}{2}} \quad (16)$$

where σ_{p1} (σ_{p2}) is computed with the $+$ ($-$) sign. The closer Θ is to 45° and the smaller the width of the distribution, σ_{p2} , the better is the agreement between two collocated data sets.

3.2. Analysis of Collocated Sets of H_s

Two typical scatter diagrams of H_s^W collocated to H_s^T and to H_s^E are presented from May 1993 (Figure 2). The number of entries is very large, namely, 42,000 and 27,000. Values of H_s below 0.5 m are discarded because they are below the precision of the altimeter measurement.

The slopes of the different line fits range from 1.16 to 1.41 for the distribution of H_s^W and H_s^T (Figure 2a). The corresponding intercepts with the y axis lie between -0.29 and -0.94 . In other words, WAM underestimates H_s being higher than 3 m and overestimates H_s being smaller than 1.5 m compared to H_s^T . On the other hand, H_s^E and H_s^W agree quite closely, which is expressed by slopes of about one and intercepts of about zero (Figure 2b). Note that the slope $b_{yx} = 0.91$ of the first regression line suggests an overestimation of the high sea states by WAM compared to H_s^E , whereas the slope $b_{xy} = 1.11$ of the second regression line suggests the reverse.

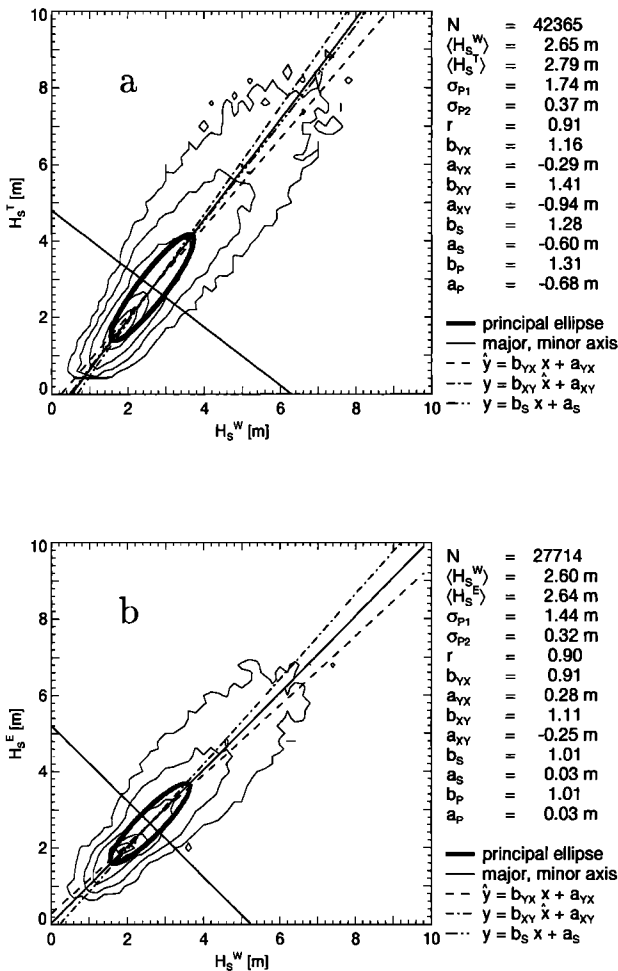


Figure 2. Scatter diagrams of global H_s from WAM (H_s^W) collocated to (a) TOPEX altimeter (H_s^T) and (b) ERS-1 altimeter (H_s^E) for May 1993. Data are binned into 0.2×0.2 m boxes, and contour lines are for: three entries and 2, 10, 40, and 70% of the maximum number of entries. The different regression lines and their coefficients are included. The half-axes of the ellipse are equal to σ_{p1} and σ_{p2} .

The range of global H_s , which is expressed by the global principal rms deviations σ_{p1} shows a weak annual cycle (Figure 3). In general, the distribution of H_s^W and H_s^T is broader by more than 10% in both principal directions compared to that of H_s^W and H_s^E . The range of H_s seen by TOPEX is larger than that seen by the ERS-1 altimeter throughout 1993. The maximum is found for July 1993 and the minimum for November 1993. The maximum (minimum) is caused by the high (low) sea states of the southern hemisphere winter (summer) which conceals the concurrent low (high) sea states of the northern hemisphere summer (winter). The annual cycle of the global H_s range does not follow a smooth sinusoidal change but exhibits some additional natural variability. The additional variability, as seen for instance, by the small dip in April 1993 (Figure 3), may not be ascribed to the different sampling of H_s^T and H_s^E because the same small dip is visible in both time series.

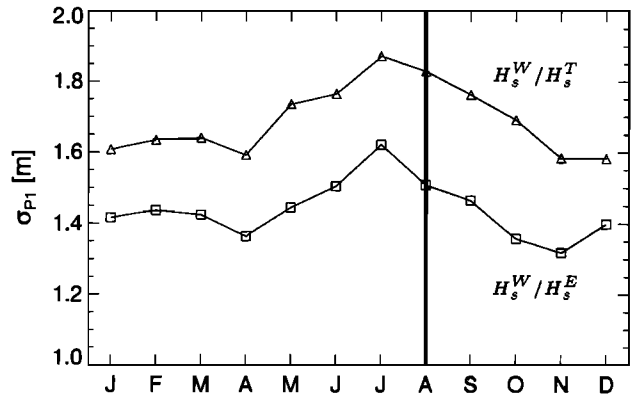


Figure 3. Time series of monthly major principal rms deviations σ_{p1} of global H_s from WAM model collocated to TOPEX altimeter (triangles) and to ERS-1 altimeter (squares) for 1993. The vertical line marks the start of data assimilation into WAM.

The monthly biases of H_s^E minus H_s^W and of H_s^T minus H_s^W show variations (Figure 4) of different origin. The large variation in spring 1993 may largely be attributed to an overestimation of H_s^W in the northern latitudes. In spring 1993 some very strong storms occurred in the North Atlantic which might be overestimated as experiences from wave data assimilation suggest [Bauer et al., 1995; S. Hasselmann et al., Assimilation of 2-D wave spectra retrieved from ERS-1 SAR wave mode image spectra into the WAM model, submitted to *Journal of Geophysical Research*, 1997]. In the second half of 1993 the biases remain about constant, with H_s^E and H_s^T being larger by 2 and 11 cm, respectively. The assimilation of H_s^E into WAM since August 16, 1993, induces hardly a change of the bias.

The slopes b_p of the major principal axes from the distributions of H_s^W and H_s^T are about 0.3 larger than those of H_s^W and H_s^E (Figure 5). Through the first half of 1993 the slopes of both bivariate distributions are nearly constant and in August, b_p increases by about

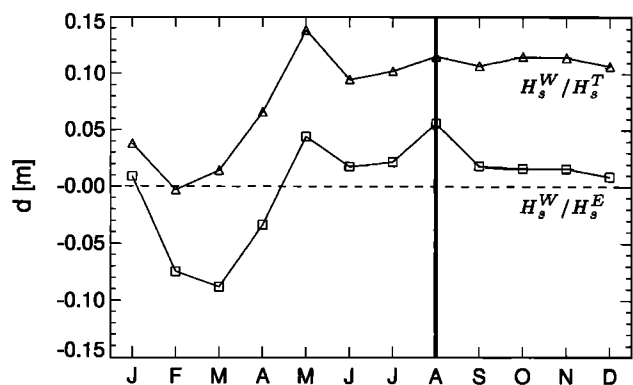


Figure 4. Time series of monthly biases d of global H_s from WAM model collocated to TOPEX altimeter (triangles) and to ERS-1 altimeter (squares) for 1993. The vertical line marks the start of data assimilation into WAM.

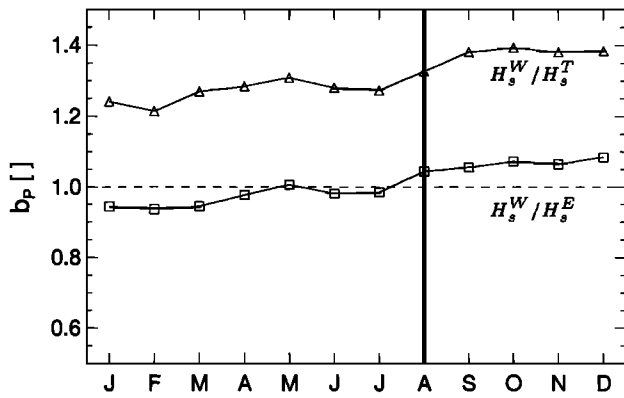


Figure 5. Time series of monthly slopes b_p of the major principal axes of global H_s from WAM model collocated to TOPEX altimeter (triangles) and to ERS-1 altimeter (squares) for 1993. The vertical line marks the start of data assimilation into WAM.

0.1. The increase of b_p is induced by the assimilation of H_s^E , which causes a reduction of the high sea states of WAM, leading to a slight rotation of the data distribution.

The correlation coefficient from H_s^W and H_s^T and from H_s^W and H_s^E varies between 0.88 and 0.92 from January to July (Figure 6). In January, April, May, and July 1993, H_s^W corresponds better with H_s^T than with H_s^E on the confidence level of 90%, and in the other months, the reverse holds. As shown before, the correlation coefficient varies through a combination of fluctuations in $\langle \varepsilon^2 \rangle$, s_{xx} , b , and $\langle x\varepsilon \rangle$, whereas the width of the bivariate distributions (Figure 7) indicates that H_s^W and H_s^E always agree better (see also Figure 2b). Therefore the evaluation of the agreement between two data sets from r alone might be misleading.

The assimilation of H_s^E into WAM causes r to increase substantially with maximum values of 0.97 for

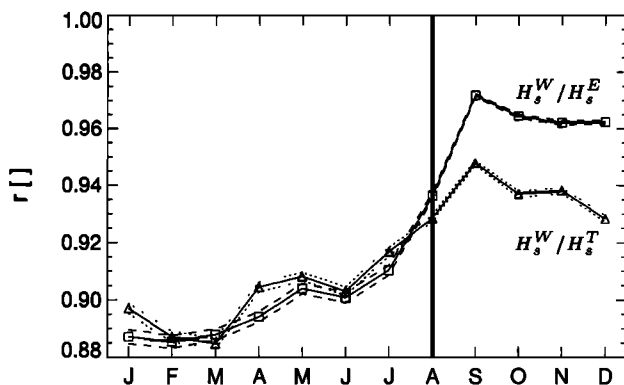


Figure 6. Time series of monthly correlation coefficients r with 90% confidence intervals of global H_s from WAM model collocated to TOPEX altimeter (triangles, confidence intervals dotted) and to ERS-1 altimeter (squares, confidence intervals dashed) for 1993. The vertical line marks the start of data assimilation into WAM.

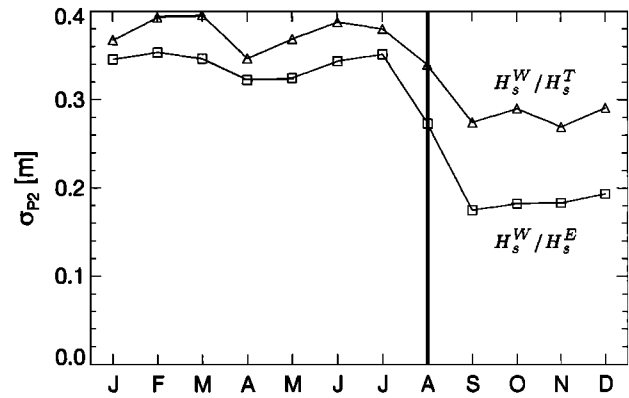


Figure 7. Time series of monthly minor principal rms deviations σ_{p2} of global H_s from WAM model collocated to TOPEX altimeter (triangles) and to ERS-1 altimeter (squares) for 1993. The vertical line marks the start of data assimilation into WAM.

H_s^W and H_s^E and of 0.95 for H_s^W and H_s^T . The impact of the assimilation may be regarded positive as the correlation of H_s^W increases significantly against the independent H_s^T data sets. The slight decrease of r after September 1993 may be related to fluctuations mentioned before. The positive impact of the assimilation of H_s^E into WAM is even more clearly reflected by the reduction of σ_{p2} (Figure 7). The σ_{p2} reduces from 35 cm to half its value for H_s^W and H_s^E and reduces from 38 cm to three-quarter for H_s^W and H_s^T .

4. Statistics of Univariate Distributions of H_s

4.1. General Considerations

The random (positive) wave heights of sea surface waves which obey linear wave theory are characterized by the Rayleigh distribution. Nonlinear contributions to the distribution of wave heights are mostly negligible. This can be inferred from investigations on whether non-Gaussian contributions are relevant for the retrieval of geophysical parameters from the backscatter of the sea surface as discussed by Srokosz [1990].

If the wave heights are Rayleigh distributed, then it is seen analytically that $H_{1/3}$, defined as the mean over the upper third of the wave heights, is identical to the significant wave height H_s . As shown before, $H_s = 4\sqrt{E}$, where the energy E is the integral over the spectral wave energy density normalized with the density of water and the acceleration of gravity. Since H_s and the wave heights are nonlinearly related, the distribution of H_s is expected to deviate from a Rayleigh distribution. A histogram of H_s sampled from large space and time regions is (usually) unimodal and positively skewed but is more sharply peaked than the Rayleigh distribution density.

Unimodal distributions are characterized by the first four moments: mean, variance, skewness, and kurtosis. The third moment measures the asymmetry, and the

fourth the peakedness of the distribution density. The third and the fourth moment remain unchanged with respect to linear transformations of the data. Unfortunately, the errors of the higher moments grow with the order of the moments. Linear moments of order statistics (hereafter called L moments) are favorable because their errors depend linearly on the error of the data and they are quite robust against possible large data errors. Furthermore, L moments are useful to determine an appropriate empirical distribution function which fits the data [Hosking, 1990].

The L moment λ_l is defined as the integral over the quantile function $x(F)$ weighted with shifted Legendre polynomials P_m^*

$$\lambda_l = \int_0^1 x(F) P_{l-1}^*(F) dF \quad l = 1, 2, \dots \quad (17)$$

$$P_m^*(F) = \sum_{k=0}^m (-1)^{m-k} \binom{m}{k} \binom{m+k}{k} F^k \quad (18)$$

The quantile function is the inverted (cumulative) distribution function. Substituting (18) into (17) yields the following expressions for the first four linear moments:

$$\lambda_1 = \int_0^1 x(F) dF \quad (19)$$

$$\lambda_2 = \int_0^1 x(F) (2F - 1) dF \quad (20)$$

$$\lambda_3 = \int_0^1 x(F) (6F^2 - 6F + 1) dF \quad (21)$$

$$\lambda_4 = \int_0^1 x(F) (20F^3 - 30F^2 + 12F - 1) dF \quad (22)$$

L moments have the same meaning as conventional moments. The first conventional moment and the first L moment are even identical. L moments of order higher than two are scaled usually with the second L moment

$$\tau_l = \frac{\lambda_l}{\lambda_2} \quad l \geq 3 \quad (23)$$

The sizes of τ_l range between 0 to 1 in contrast to normalized conventional moments which can grow unlimited.

The distributions of H_s have been fitted to various empirical functions. It has been found out that the lognormal (GNO) and the general extreme value (GEV) distribution are most suitable. The lognormal distribution

$$F_{GNO}(x) = \frac{1}{\sigma\sqrt{2\pi}} \int_{-\infty}^x \frac{1}{x'} \exp\left(-\frac{(\log(x' - \xi) - \mu)^2}{2\sigma^2}\right) dx' \quad (24)$$

is a natural distribution function for nonsymmetrically distributed variables where μ denotes the mean and σ denotes the rms deviation of the corresponding normal

distribution, and ξ is an offset. The GNO distribution is known in general to result from multiplicative concurrence of random variables and may therefore be suitable to describe distributions of H_s . Neu [1984] found that H_s from synoptic charts based on visual and instrumental observations was described extremely well by the lognormal distribution.

The GEV distribution function is given by

$$F_{GEV}(x) = \exp\left[-\left(1 - \frac{\beta}{\alpha}(x - \xi)\right)^{1/\beta}\right] \quad (25)$$

The location ξ , the scale α , and the shape β are easily inferred from the first three L moments. The GEV distribution function with $\beta < 0$ is defined for $x > \alpha/\beta + \xi$.

4.2. Analysis of Statistical Moments

Before the fitted empirical distribution functions are presented, we compare the first four moments of the data sets listed in Table 1. The frequency distributions of the regional H_s data sets show seasonal variations. This is reflected in the first and the second moments, while the third and the fourth moments only show small changes. This suggests that the H_s distributions are consistent with one empirical function. To test this, the moments are computed from latitudinal subsets. Each data set is divided into three subsets, one for the latitudes north of 23°N, one south of 23°S, and one for the latitudes between. Fixing the outer boundaries to 60° latitude yields negligible small differences of the moments. The data sets of each region are arranged into six groups to direct the attention to the following questions:

1. How large are the differences between altimeter H_s and collocated H_s^W and can they be explained?
2. What was the effect of updating WAM from cycle 3 to cycle 4?
3. What change was brought by the new algorithm of the ERS-1 altimeter in January 1994?
4. How large is the interannual variability between two successive years (1993, 1994) inferred from H_s^T ?
5. How stable are the moments with respect to different spatial sampling using H_s from WAM of 1993?

To answer these questions, time series of the means and the standard deviations are presented in Figure 8 and Figure 9, respectively. Changes of the shapes of the frequency distributions can be inferred from the third and the fourth moment. Figure 10 shows the annual means with rms of the normalized third (τ_3) and fourth (τ_4) moments from linear order statistics which show much less variations compared to the corresponding conventional moments. The advantage of displaying

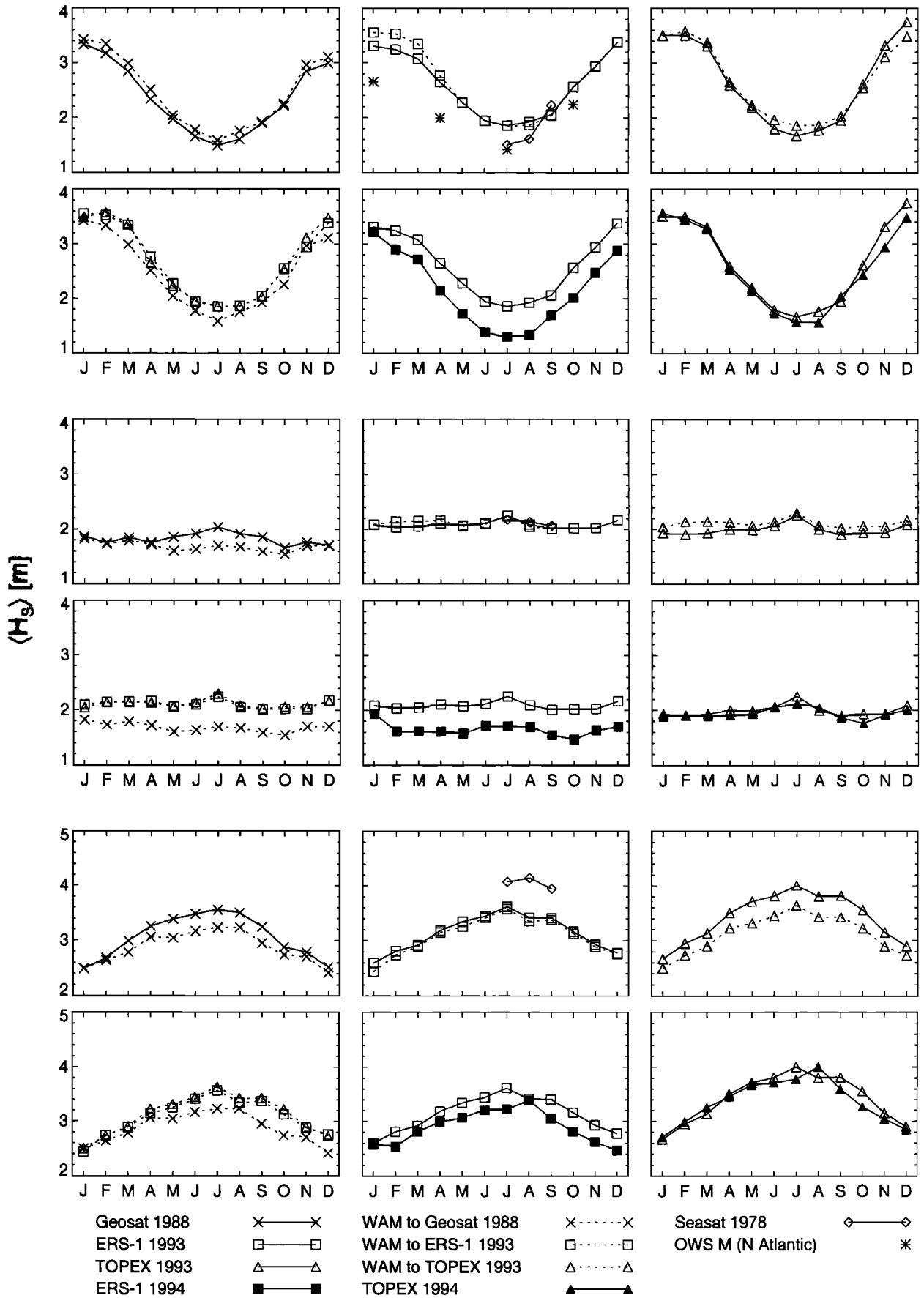


Figure 8. Time series of monthly means of H_s from altimeter and WAM model for northern (N1 - N6), low (T1 - T6), and southern latitudes (S1 - S6).

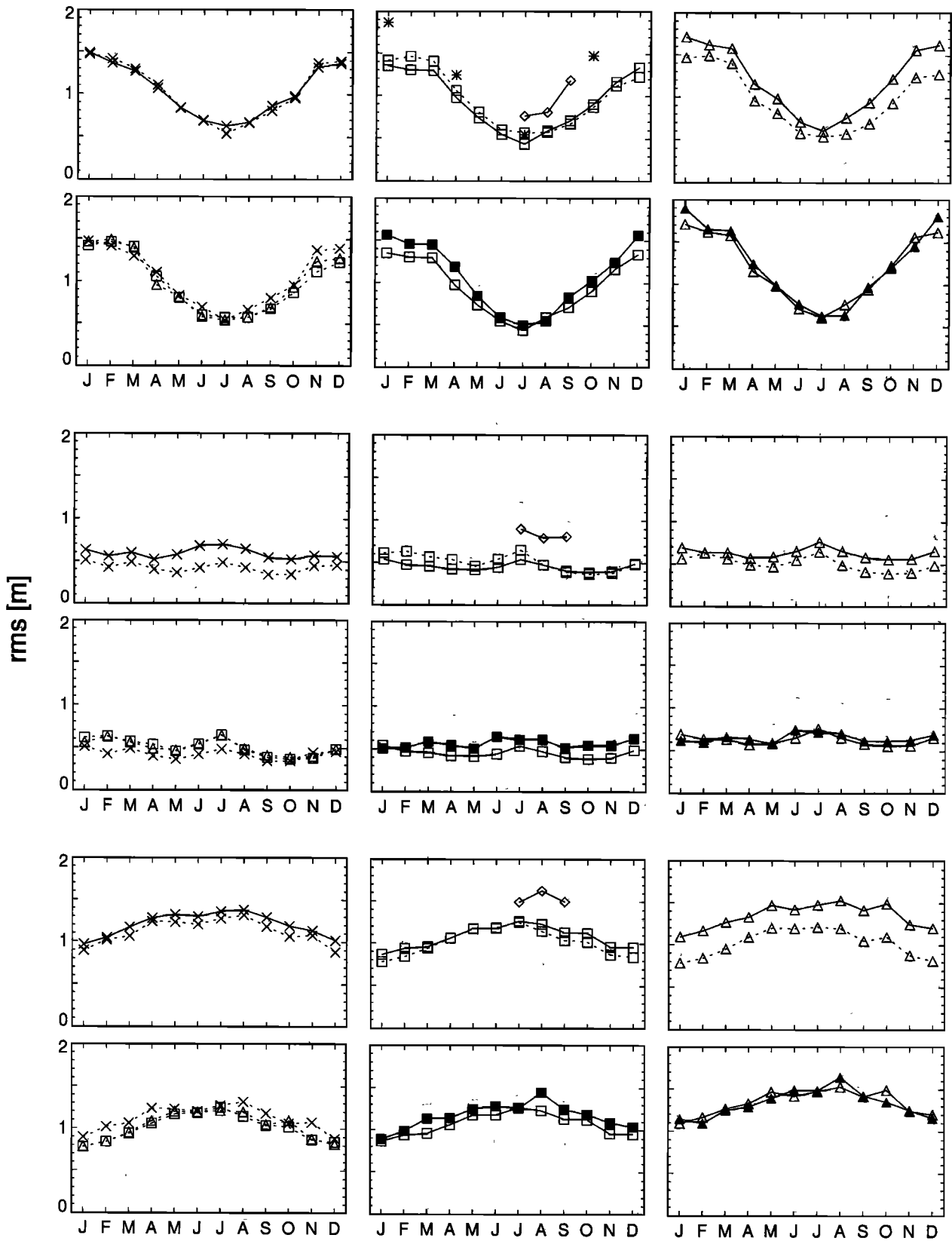


Figure 9. Time series of monthly rms deviations of H_s from altimeter and WAM model for northern (N1 - N6), low (T1 - T6), and southern latitudes (S1 - S6). For legend, see Figure 8.

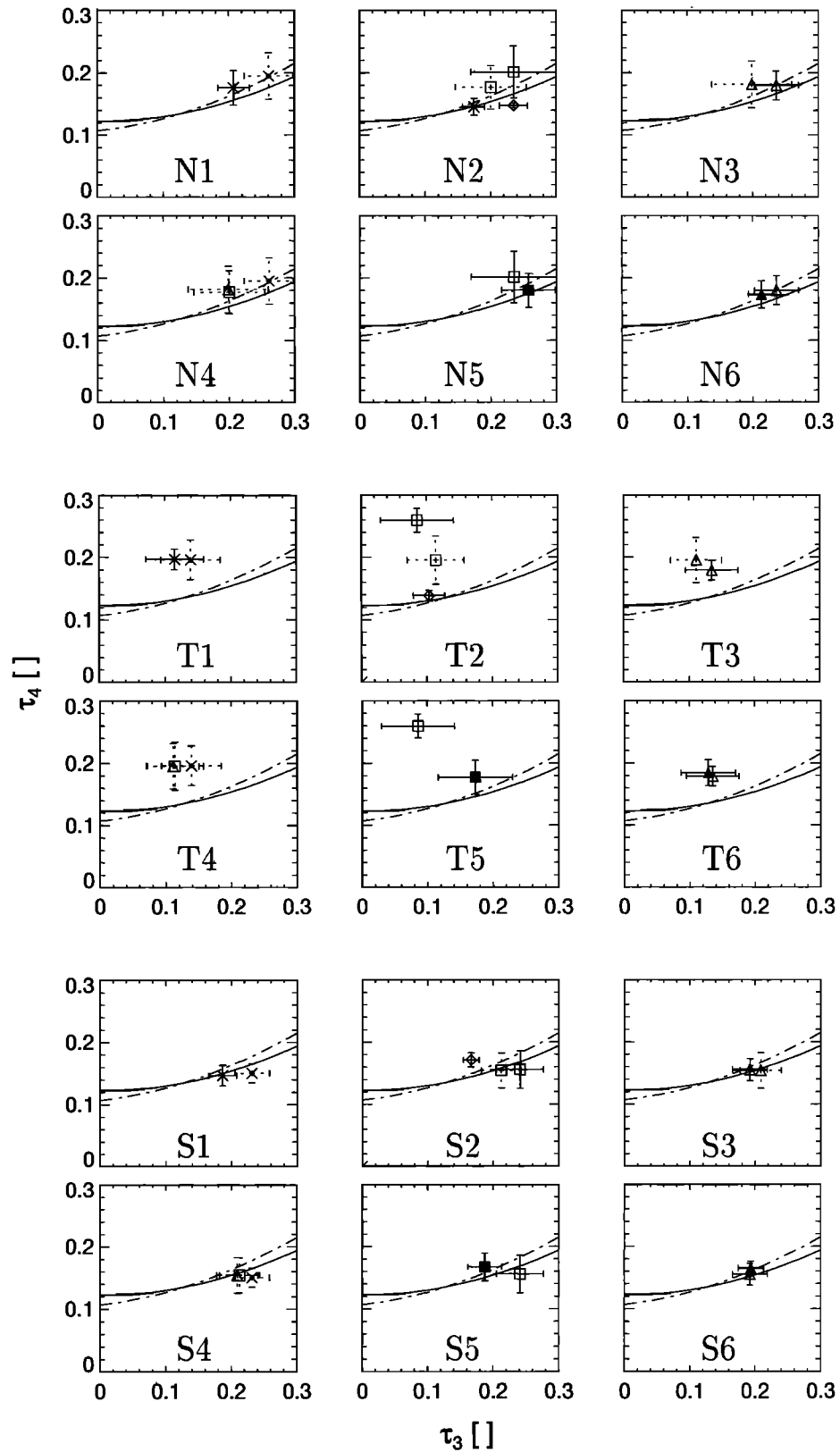


Figure 10. Annual mean fourth (τ_4) versus third (τ_3) linear moments of H_s from altimeter and WAM model for northern (N1 - N6), low (T1 - T6), and southern latitudes (S1 - S6). The standard deviations of annual means are indicated by error bars. The relationships of τ_3 and τ_4 for GNO (solid) and GEV (dashed) are shown for comparison. For legend, see Figure 8.

τ_3 and τ_4 together in one diagram is that the consistency with the GNO or the GEV distribution function can be seen directly. The moments are displayed in Figures 8-10, where each figure shows six panels for six groups of data sets separated into northern, tropical, and southern data which are marked by Nn, Tn, and Sn with $n = 1 \dots 6$.

4.2.1. Monthly means (Figure 8). The means of H_s^W are larger than those of H_s^G in the northern (N1) and lower in the southern latitudes (S1). In the low latitudes, H_s^G exceeds H_s^W from May to September by more than 20 cm, revealing that too little swell is generated by WAM in the southern winter (T1). The means of collocated H_s^W and H_s^T differ inhomogeneously. The means are about the same in the north (N3), are larger for H_s^W in the low latitudes (T3), and are larger for H_s^T by as much as 40 cm in the south (S3). The underestimation of H_s in the south by WAM compared with H_s^G and H_s^T can be attributed to an incorrect model forcing in the southern latitudes [Bauer *et al.*, 1992; Romeiser, 1993].

The means of H_s^W are larger for 1993 (WAM cycle 4) than for 1988 (WAM cycle 3), indicating that the modeling of swell energy has improved (N4, T4, S4) but the swell energy still remains too weak in the south (S3). The monthly differences in 1993 between the two differently sampled sets of H_s^W reach a maximum of 0.1 m, which may be regarded as negligible in this study.

The means of H_s^E decrease significantly from 1993 and 1994 (N5, T5, S5). This change must mainly be induced by the modified sensor algorithm because it cannot be explained with natural interannual variations as seen from H_s^T (N6, T6, S6).

4.2.2. Monthly rms deviations (Figure 9). The rms values of H_s^T (e.g., N6) exhibit a larger variability than all other data sets, except for rms of H_s^S (e.g., S2). The interannual rms changes between 1993 and 1994 vary randomly (see T6), but rms of H_s^E increases slightly from 1993 to 1994 (T5). This increase of rms of H_s^E is in contrast to the decrease of the mean of H_s^E . The change of WAM from cycle 3 to cycle 4 has no significant effect on the rms values (N4, T4, S4).

4.2.3. Monthly third and fourth L moments (Figure 10). The distribution densities of H_s are more skewed and broader in the higher latitudes than in the lower latitudes. This is expressed by larger values of τ_3 and smaller values of τ_4 in the higher latitudes. Superimposed on these regional variations are temporal variations which are smallest in the south.

The distribution of H_s^W of cycle 4 is slightly less skewed than that of cycle 3 (N4, T4, S4). The L moments of H_s^S are significantly different from the other data sets (e.g., S2). The L moments of H_s^E indicate distinct changes from 1993 to 1994 which show that the change of the sensor algorithm has a nonlinear effect (N5, T5, S5).

The third and fourth L moments of the data sets are compared with those associated with the GNO (24) and the GEV (25) distribution. Linear moments of H_s^G , H_s^W , and H_s^T from the southern region (S1, S3, S4) agree rather closely with the L moments of the GNO distribution. Also τ_3 and τ_4 of the in situ data of OWS M (N2) show small scattering and agree well with the GNO distribution. But the L moments of H_s^G , H_s^W , and H_s^T from the northern region (N1, N3, N4) resemble more the L moments of the GEV distribution. In the low latitudes neither the modeled nor the altimeter data are seen to correspond to the GNO or the GEV distribution (T1, T2, T3).

4.3. Analysis of Probability Distributions

Histograms of H_s of the altimeters are compared with those of the WAM model for the three regions and for the four seasons. The largest widths of the histograms are seen from the northern winter data which are depicted as an example in Figure 11. Since H_s^S is available only from July to October 1978, the histogram is shown from the southern winter data. Each H_s histogram is shown together with the fitted GEV and the GNO distribution.

In searching for the most suitable empirical distribution function, the data of H_s^S and H_s^E (1993) should not be considered. The histogram of H_s^S shows an abnormal tri-modal shape (Figure 11f). The two secondary modes at 2 and 6 m reflect a defect of the measured signals [cf. Carter *et al.*, 1992; Freilich and Dunbar, 1993]. The distribution density from H_s^E of 1993 shows an exceptional sharp peak at 2 m (Figure 11c). This sharp peak is visible in all histograms of H_s^E of 1993, but in none of the histograms from the other data sets. The peak is caused obviously by an error in the data processing. The peak is removed after the implementation of the new sensor algorithm in 1994 (Figure 11d), but instead an unexpected dip below the peak appears.

Although the number of samples which enters each histogram is large ($\sim 20,000$ entries), the histograms of H_s^G and H_s^E are rather ragged compared to the quite smooth histograms of H_s^T and H_s^W . The three fitted distribution functions show negligibly small differences if the histograms are smooth (Figures 11b, 11e). The frequency distribution of H_s is better simulated by the GNO distribution with three parameters than by GNO with two parameters (setting $\xi=0$) in those cases in which low values of H_s are underrepresented.

From the available data sets, it cannot be proven whether distributions of H_s are strictly consistent with the GNO distribution. In most cases the data fail to pass the Kolmogorov-Smirnov test. This is mainly caused by the large data sets, which leads to very narrow confidence intervals. The GNO distribution fits the H_s distributions slightly better from the southern re-

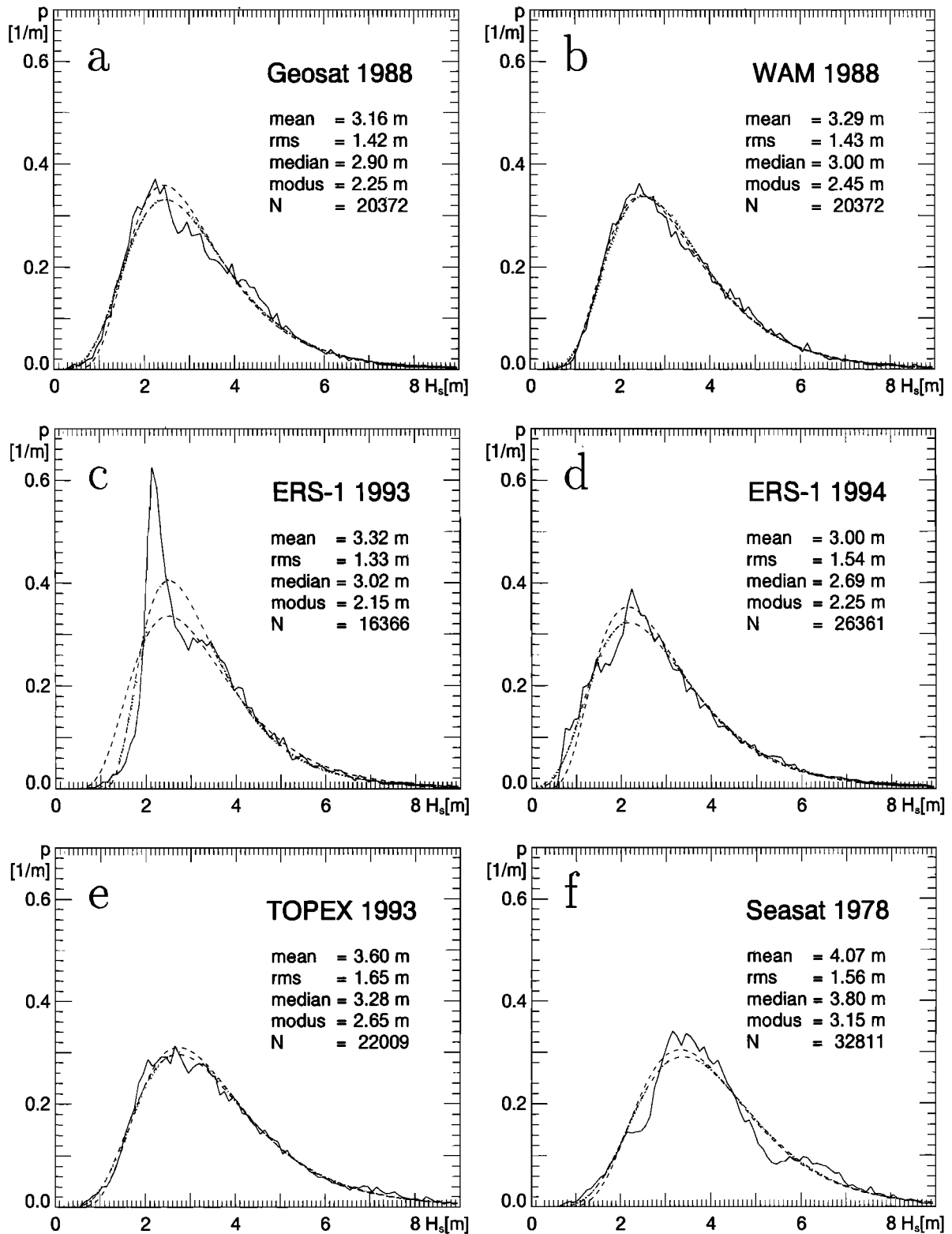


Figure 11. Histograms of H_s from (a) Geosat 1988, (b) WAM 1988, (c) ERS-1 1993, (d) ERS-1 1994, and (e) TOPEX 1993, obtained for winter (December - February) from the northern latitudes, and from (f) Seasat (1978) for winter (July - September) from the southern latitudes. Distribution densities fitted to each data set are GEV (dotted), two-parameter GNO (dashed), and three-parameter GNO (dash-dotted). Mean, rms, median, modus, and number of samples N are given for each data set.

gion, and the GEV distribution those from the northern region.

5. Conclusions

Global H_s data over several years of altimeter measurements, of WAM model calculations, and of in situ measurements from the North Atlantic by OWS M are analyzed to infer general statistical properties useful for data evaluation. Differences in the statistics are difficult to assess, as they are often small with respect to the seasonal variability. The combined analysis of bivariate and univariate distributions is shown to contribute to the assessment of the absolute quality of H_s data sets.

Collocated data sets can be compared adequately by the major and minor principal axes of the elliptical data distribution and by the principal rms deviations σ_{p1} and σ_{p2} . Two data sets agree very well if the major axis has slope one and intercept zero and if σ_{p2} approaches zero. These conditions are clearly better fulfilled by the distribution of H_s^W and H_s^E than by the distribution of H_s^W and H_s^T .

However, the analysis of the univariate distributions reveals that the absolute quality of H_s^E suffers from shortcomings. The H_s distributions from Geosat, TOPEX and WAM from the extratropical regions are consistent with the GNO or the GEV distribution or both. The suitability of the GNO distribution to describe H_s distributions is supported by the in situ data of OWS M, which are known to be of good quality. The histograms of H_s from the Seasat and the ERS-1 altimeter show abnormal shapes, reflecting a reduced quality.

The H_s distributions from low latitudes cannot be described by the GNO or the GEV distribution. This might be explained with the frequency distribution of surface wind fields, which is different in the low latitudes compared to the high latitudes [Bauer, 1996].

The available H_s data sets are found to be too inhomogeneous to study interannual changes. In some case the changes can be attributed to differences in the data processing. This is evident, for instance, when the corrections to the ERS-1 altimeter algorithm and to the WAM model were implemented.

H_s of the Geosat altimeter (1988) is seen to have smaller means and rms deviations by as much as about 10% compared to H_s of the TOPEX altimeter (1993, 1994). This increase with time might be due to inconsistencies in the data and due to natural fluctuations. An increase of the global H_s^G by 13% as proposed by Carter *et al.* [1992] leads to a reversed trend in some times and in some regions. The analysis of trends as discussed, for instance, by Bacon and Carter [1991] is beyond the scope of the present study.

We conclude that H_s from satellite measurements need to be validated on a global scale and continuously in time. For this, global and continuous calculations with the WAM model are useful. However, modeled H_s

data may also have errors caused, for instance, by incorrect wind forcing. The correction of modeled H_s can be achieved, at least partly, through dynamically consistent wave data assimilation schemes. Although neither the altimeter measurements nor the modeled data are perfect, some positive impact of the assimilation of H_s^E into WAM could be demonstrated convincingly. This is inferred from the comparison against the independent and homogeneous H_s data of the TOPEX altimeter. A further improvement in global wave prediction may be achieved by assimilating spectral wave data from synthetic aperture radar. Such assimilation schemes are currently under development. The validation of these data assimilation schemes requires, however, independent data of high quality.

Acknowledgments. This study is a contribution to the research program "Klimarelevante Prozesse im System Ozean-Atmosphäre-Kryosphäre" (SFB 318) funded by the Deutsche Forschungsgemeinschaft. It was also supported by the German Space Agency (DARA) under contract 50 EE 94 13. The data were provided by ESA under the ERS-1/2 projects PP2.D1 and AO2.D109.

References

- Bacon, S., and D. J. T. Carter, Wave climate changes in the North Atlantic and North Sea, *Int. J. Climatol.*, 11, 545-558, 1991.
- Barrick, D. E., Rough surface scattering based on the specular point theory, *IEEE Trans. Antennas Propagat.*, AP-14(4), 449-454, 1968.
- Bauer, E., Characteristic frequency distributions of remotely sensed, in situ and modelled wind speeds, *Int. J. Climatol.*, 16, 1087-1102, 1996.
- Bauer, E., S. Hasselmann, K. Hasselmann, and H. C. Graber, Validation and assimilation of Seasat altimeter wave heights using the WAM wave Model, *J. Geophys. Res.*, 97, 12,671-12,682, 1992.
- Bauer, E., S. Hasselmann, and C. Brüning, Application of wave spectra retrieved from ERS-1 SAR wave mode spectra in a wind- and wave-data system, in *Proceedings of IGARSS'95*, pp. 1643-1645, Int. Geosci. and Remote Sens. Symp., Firenze, Italy, 1995.
- Bauer, E., K. Hasselmann, I. R. Young, and S. Hasselmann, Assimilation of wave data into the wave model WAM using an impulse response function method, *J. Geophys. Res.*, 101, 3801-3816, 1996.
- Callahan, P. S., C. S. Morris, and S. V. Hsiao, Comparison of TOPEX/POSEIDON σ_0 and significant wave height distributions to Geosat, *J. Geophys. Res.*, 99, 25,015-25,024, 1994.
- Cardone, V. J., H. C. Graber, R. E. Jensen, S. Hasselmann, and M. J. Caruso, In search of the true surface wind field in SWADE IOP-1: Ocean wave modelling perspective, *Global Atmos. Ocean Syst.*, 3, 107-150, 1995.
- Carter, D. J. T., P. G. Challenor, and M. A. Srokosz, An assessment of Geosat wave height and wind speed measurements, *J. Geophys. Res.*, 97, 11,383-11,392, 1992.
- Cotton, P. D., and D. J. T. Carter, Cross calibration of TOPEX, ERS-1, and Geosat wave heights, *J. Geophys. Res.*, 99, 25,025-25,033, 1994.
- Dobson, E., F. Monaldo, J. Goldhirsh, and J. Wilkerson, Validation of Geosat altimeter-derived wind speeds and significant wave heights using buoy data, *J. Geophys. Res.*, 92, 10,719-10,731, 1987.

- Fedor, L. S., and G. S. Brown, Wave height and wind speed measurements from the Seasat altimeter, *J. Geophys. Res.*, *87*, 3254-3260, 1982.
- Freilich, M. H., and R. S. Dunbar, Derivation of satellite wind model functions using operational surfaces wind analysis: An altimeter example, *J. Geophys. Res.*, *98*, 14,633-14,649, 1993.
- Gower, J. F. R., Intercalibration of wave and wind data from TOPEX/POSEIDON and moored buoys of the west coast of Canada, *J. Geophys. Res.*, *101*, 3817-3829, 1996.
- Hansen, B., and H. Günther, ERS-1 radar altimeter validation with the WAM model, ERS-1 Geophysical Validation Workshop Proceedings, *ESA WPP-36*, pp. 157-161, Eur. Space Agency, Paris, France, 1992.
- Hosking, J. R. M., L-moments: Analysis and estimation of distributions using linear combinations of order statistics, *J. R. Statist. Soc., Ser. B*, *52*, 105-124, 1990.
- Janssen, P. A. E. M., Quasi-linear theory of wind wave generation applied to wave forecasting, *J. Phys. Oceanogr.*, *22*, 1631-1642, 1991.
- Komen, G. J., L. Calvaleri, M. Donelan, K. Hasselmann, S. Hasselmann, and P. A. E. M. Janssen, *Dynamics and Modelling of Ocean Waves*, 560 pp., Cambridge Univ. Press, New York, 1994.
- Lionello, P., H. Günther, and B. Hansen, A sequential assimilation scheme applied to global wave analysis and prediction, *J. of Mar. Syst.*, *6*, 87-107, 1995.
- Monaldo, F., Expected differences between buoy and radar altimeter estimates of wind speed and significant wave height and their implications on buoy-altimeter comparisons, *J. Geophys. Res.*, *93*, 2285-2302, 1988.
- Neu, H. J. A., Interannual variations and longer-term changes in the sea state of the North Atlantic from 1970 to 1982, *J. Geophys. Res.*, *89*, 6397-6402, 1984.
- Queffeuou, P., Seasat wave height measurements: A comparison with sea truth data and a wave forecasting model: Application to the geographic distribution of strong sea states in storms, *J. Geophys. Res.*, *88*, 1779-1788, 1983.
- Queffeuou, P., and A. Bentamy, Evaluation of wind and wave measurements from the TOBIS buoy network during RENE-91, ERS-1 Geophysical Validation Workshop Proceedings, *ESA WPP-36*, pp. 29-34, Eur. Space Agency, Paris, France, 1992.
- Queffeuou, P. and J. M. Lefevre, Validation of ERS-1 altimeter wave and wind fast delivery product, ERS-1 Geophysical Validation Workshop Proceedings, *ESA WPP-36*, pp. 163-168, Eur. Space Agency, Paris, France, 1992.
- Romeiser, R., Global validation of the wave model WAM over a one-year period using Geosat wave height data, *J. Geophys. Res.*, *98*, 4713-4726, 1993.
- Srokosz, M. A., Wave statistics, in *Surface Waves and Fluxes*, edited by G. L. Geernaert and W. J. Plant, vol. 1, pp. 285-332, Kluwer Acad., Norwell, Mass., 1990.
- Staabs, C., Vergleich von Wellenhöhen berechnet mit dem Seegangmodell WAM mit Daten der Radarhöhenmesser an Bord der Satelliten ERS-1 und TOPEX/POSEIDON, Master thesis, 88 pp., Univ. Hamburg, Hamburg, Germany, 1994.
- Tournadre, J., and R. Ezraty, Local climatology of wind and sea state by means of satellite radar altimeter measurements, *J. Geophys. Res.*, *95*, 18,255-18,268, 1990.
- WAMDI Group (S. Hasselmann, K. Hasselmann, E. Bauer, P. A. E. M. Janssen, G. J. Komen, L. Bertotti, P. Lionello, A. Guillaume, V. C. Cardone, J. A. Greenwood, M. Reistad, L. Zambresky, and J. A. Ewing), The WAM model - A third generation ocean wave prediction model, *J. Phys. Oceanogr.*, *14*, 1775-1810, 1988.
- Zambresky, L., An evaluation of two WAM hindcasts for LEWEX, in *Directional Ocean Wave Spectra*, edited by R. C. Beal, pp. 167-172, Cambridge Univ. Press, New York, 1991.

E. Bauer, Potsdam Institute for Climate Impact Research, P.O. Box 601203, 14412 Potsdam, Germany. (e-mail: eva.bauer@pik-potsdam.de)

C. Staabs, Institut für Meereskunde, Universität Hamburg, Troplowitzstr. 7, 22529 Hamburg, Germany. (e-mail: staabs@dkrz.de)

(Received January 9, 1997; revised August 11, 1997; accepted September 8, 1997.)